SCIENTIFIC REPORTS

OPEN

Enhanced photoelectrochemical and photocatalytic behaviors of MFe$_2$O$_4$ (M = Ni, Co, Zn and Sr) modified TiO$_2$ nanorod arrays

Xin Gao*, Xiangxuan Liu*, Zuoming Zhu, Xuanjun Wang & Zheng Xie

Modified TiO$_2$ nanomaterials are considered to be promising in energy conversion and ferrites modification may be one of the most efficient modifications. In this research, various ferrites, incorporated with various cations (MFe$_2$O$_4$, M = Ni, Co, Zn, and Sr), are utilized to modify the well aligned TiO$_2$ nanorod arrays (NRAs), which is synthesized by hydrothermal method. It is found that all MFe$_2$O$_4$/TiO$_2$ NRAs show obvious red shift into the visible light region compared with the TiO$_2$ NRAs. In particular, NiFe$_2$O$_4$ modification is demonstrated to be the best way to enhance the photoelectrochemical and photocatalytic activity of TiO$_2$ NRAs. Furthermore, the separation and transfer of charge carriers after MFe$_2$O$_4$ modification are clarified by electrochemical impedance spectroscopy measurements. Finally, the underlying mechanism accounting for the enhanced photocatalytic activity of MFe$_2$O$_4$/TiO$_2$ NRAs is proposed. Through comparison among different transition metals modified TiO$_2$ with the same synthesis process and under the same evaluating condition, this work may provide new insight in designing modified TiO$_2$ nanomaterials as visible light active photocatalysts.

In recent years, titanium oxide (TiO$_2$), as a "green" photocatalyst, has attracted lots of attention worldwide due to its low cost, nontoxicity and excellent photochemical stability[1]. However, due to the rapid recombination of photogenerated electron-hole pairs as well as the lack of visible light absorption[2], the photocatalytic and photo-electrochemical efficiency of pure TiO$_2$ is quite limited. Pure TiO$_2$, with bandgap of *ca*. 3.0 to 3.2 e*V*, can only be excited under UV light irradiation, which comprises only ~5% of the total solar radiation, so, application of the unmodified TiO$_2$ in solar energy conversion is far limited[3]. Besides, the excited charge carriers in TiO$_2$ can recombine quickly and more than 90% of the recombination processes take place in $10\,ns$[4], therefore, only a little fraction of the excited carriers can transfer to the surface of TiO$_2$ and take part in the following photocatalytic process. To make full use of solar energy and reduce the recombination rate, many attempts have been made, such as doping with metal/nonmetal atoms and deposition of metals. Though the aforementioned methods can partly improve the photocatalytic as well as photoelectrochemical activity of TiO$_2$, some problems remain unresolved. For example, doped TiO$_2$ may suffer from thermal instability, photo corrosion, lattice distortion, while metal loading may result in an increase in the carrier-recombination probability[5]. In this case, one of the promising strategies is to couple TiO$_2$ with other narrow band gap semiconductors, which are capable of harvesting photons in the visible light region. Recently, CdS with a low band gap (*ca*. 2.4 eV) was studied intensively to improve the visible light uitilizion of TiO$_2$. However, its application is also hindered due to the low photostability[6]. In view of this, transition metal ferrites with molecular formula of MFe$_2$O$_4$ (M = Zn, Co, Ni, etc.) go into the vision of researchers considering its outstanding attributes. Firstly, these materials possess an important characteristic of narrow band gap, which could absorb the visible light efficiently[7] and thus promote the photocatalytic reactions. Secondly, MFe$_2$O$_4$ has a good electrical conductivity due to the electron hopping process between different valence states of metals in O-sites, which is beneficial for the transfer of charge carriers[8,9]. Furthermore, transition metal ferrites have many intriguing advantages such as well stability against photocorrosion, good superparamagnetic properties, low toxicity, easy preparation, high adsorption ability, low cost, and abundant resources[10–12]. So far, most of the researches are focused on separation of TiO$_2$ powders from treated water by employing its

High-Tech Institute of Xi'an, Xi'an, 710025, China. *These authors contributed equally to this work. Correspondence and requests for materials should be addressed to Z.X. (email: xiezheng10@tsinghua.org.cn)

magnetic property of transition metal ferrites[13–15]. It is scarce on study of the visible responsiveness of MFe_2O_4 to increase utilization of solar energy as well as to enhance the photoelectrochemical and photocatalytic performance of TiO_2.

$ZnFe_2O_4$, with a relatively small band-gap (ca. 1.9 eV)[16], is the most frequently studied to modify TiO_2 in enhancing the photoelectrochemical capacity. Yuan et.al observed that the $ZnFe_2O_4/TiO_2$ nanocomposite is more effective as a photocatalyst in the phenol degradation than pure TiO_2. However the mechanism of the enhanced photoactivity of the $ZnFe_2O_4/TiO_2$ composite is still needed to be further understood[17]. Furthermore, the following researches proposed similar theory to explain the role of $ZnFe_2O_4$ in enhancing photoactivity of TiO_2[18,19], that is, the adoption of $ZnFe_2O_4$ makes the $ZnFe_2O_4/TiO_2$ composite could use visible light, and the good match of band edges between $ZnFe_2O_4$ and TiO_2 is in favor of charge carriers separating effectively. Reports about other MFe_2O_4 modified TiO_2, such as $NiFe_2O_4/TiO_2$, $Mn_{0.5}Zn_{0.5}Fe_2O_4/TiO_2$, $MgFe_2O_4/TiO_2$ and $CuFe_2O_4/TiO_2$ all show higher photoelectrochemical and photocatalytic performance[20–23]. It seems that MFe_2O_4 is such a promising material to improve the photoelectrochemical and photocatalytic performance of TiO_2. However, the comparison among the photoelectrochemical and photocatalytic performances of transition metal ferrites modified TiO_2 reported in the literatures is extremely difficult, because the experimental conditions were very different, such as catalysts synthesis process, light irradiation wavelength, reactor geometric configuration, catalyst loading and so on. Moreover, the origin and the crystalline structure of TiO_2, which strongly affect its electronic and photoactivity, are also different. Therefore, the same condition should be taken into consideration when assessing the real effect of transition metal ferrites on the photoactivity of TiO_2, such as using the same bare TiO_2 as the starting material, taking the same procedure to modify TiO_2 by transition metal ferrites, and finally evaluating their performances with unified standards. $NiFe_2O_4$, $CoFe_2O_4$, $ZnFe_2O_4$ and $SrFe_2O_4$ are four common transition metal ferrites which have been frequently studied with their magnetism, but except for $ZnFe_2O_4$, the other three are not common in modifying TiO_2 to enhance its photoactivity, therefore, we select the four as research objects, making a comparision between the common one ($ZnFe_2O_4/TiO_2$) and the uncommon ones ($CoFe_2O_4$, $ZnFe_2O_4$ and $SrFe_2O_4$ modified TiO_2).

In addition to incorporate other materials to modify TiO_2, structural design is another important method to enhance the photoactivity of TiO_2. One-dimensional (1D) nanostructure such as nanowire, nanotube, nanorod have attracted lots of attention due to the unique physical and chemical properties. 1D TiO_2 nanomaterials possess all the typical features of TiO_2 nanoparticles[24]. Electron diffusion length (up to ~100 μm) can be prolonged by using vertically aligned 1D nanostructures and excited electrons can easily pass along 1D nanostructure to the transparent conducting oxide electrode[25,26], which facilitate charge transfer and promote charge separating efficiently[20,27]. However, the relatively low specific surface area on a smooth surface of 1D nanostructures may decrease the absorption ability and a single crystal phase of 1D nanostructures may pose certain constraints on the photoelectrochemical performance[24,28]. Fortunately, these disadvantages can be surmouned by introducing the second phase, i.e., doping metals/nonmetals or forming heterjunctions. Among1D nanostructures, 1D nanorod arrays with large area can be easily obtained by hydrothermal method, which is facile, economic and controllable[29]. Therefore, coupling the traits of one-dimensional TiO_2 nanorods (TiO_2 NRAs) and visible light responsive MFe_2O_4 nanoparticles seems to be a promising way to enhance the solar energy conversion efficiency of TiO_2.

To the best of our knowledge, there is few systematic research on the photoelectrochemical and photocatalytic capacity of various MFe_2O_4 modified one-dimensional TiO_2 NRAs so far. In this study, large area uniform TiO_2 NRAs were synthesized hydrothermally and ferrites containing vaious cations (MFe_2O_4, M = Ni, Co, Zn, and Sr) were utilized to modify the as-prepared TiO_2 NRAs. The morphology, crystalline structures and optical properties as well as photoelectrochemical performances of TiO_2 NRAs and MFe_2O_4/TiO_2 NRAs were investigated. Moreover, the photocatalytic activities of the MFe_2O_4/TiO_2 NRAs were evaluated in the degradation of Cr(VI) aqueous solution under visible light irradiation. Finally, the underlying photctalytic mechanism was discussed.

Results and Discussion

Figure 1(a) displays the XRD patterns collected from the TiO_2 NRAs and MFe_2O_4/TiO_2 NRAs. It can be seen that the TiO_2 NRAs and MFe_2O_4/TiO_2 NRAs all features the characteristic peaks at $2\theta = 36.078°$, $62.750°$, $69.010°$ and $69.795°$, indicative of rutile TiO_2 (PDF NO. 21–1276). Other peaks can be attributed to the diffraction of FTO substrate. There is no typical diffraction peaks of MFe_2O_4 after modification, which may be owing to the low content of MFe_2O_4. The content of MFe_2O_4 will be discussed in the following SEM characterization.

In order to further examine the phase composition of the samples and confirm the existence of MFe_2O_4, Raman spectroscopy was employed. As is shown clearly in Fig. 1(b), there are three Raman peaks at 241.4, 445.6 and 609.5 cm^{-1} for all samples, which are assigned to the Raman active modes of rutile[30]. This result indicates that the rutile phase dominates the crystalline structure of the samples, which is in accordance with the XRD result. However, the Raman peak corresponding to MFe_2O_4 is not discernable due to the low content of MFe_2O_4. The peak at 117 cm^{-1} is due to plasma emission of the Ar^+ laser[31].

In order to further confirm the existence of MFe_2O_4, XPS measurement was carried out. The XPS survey spectra are shown in Fig. 2(a). The peaks located at the binding energies of ca. 458–464 eV, 529–531 eV, 711–725 eV and 284–288 eV in all samples are ascribed to the Ti 2p, O 1s, Fe 2p, and C 1s, respectively. On the other hand, these MFe_2O_4/TiO_2 NRAs materials also show their characteristic peaks located between 850 and 875 eV (Ni 2p) for $NiFe_2O_4/TiO_2$ NRAs, 781 and 796 eV (Co 2p) for $CoFe_2O_4/TiO_2$ NRAs, 1021 and 1044 eV (Zn 2p) for $ZnFe_2O_4/TiO_2$ NRAs, and 134 eV (Sr 2p) for $SrFe_2O_4/TiO_2$ NRAs.

As is shown in Fig. 2(b), the Ni 2p peaks of $NiFe_2O_4/TiO_2$ NRAs consist of two characteristics of Ni 2p3/2 (855.72 eV) and Ni 2p1/2 (874.12 eV)[32], indicative of the presence of Ni^{2+}. Similar to the Ni 2p peaks in $NiFe_2O_4/TiO_2$ NRAs, the Co 2p XPS spectra recorded from the $CoFe_2O_4/TiO_2$ NRAs sample, containing Co 2p3/2 (781.03 eV, Co^{2+} in Tet-site) and Co 2p1/2 (796.67 eV, Co^{2+} in Tet-site), indicate that Co^{2+} exists in the $CoFe_2O_4/TiO_2$ NRAs according to the literature reports[33]. For the $ZnFe_2O_4/TiO_2$ NRAs, the recorded Zn 2p XPS
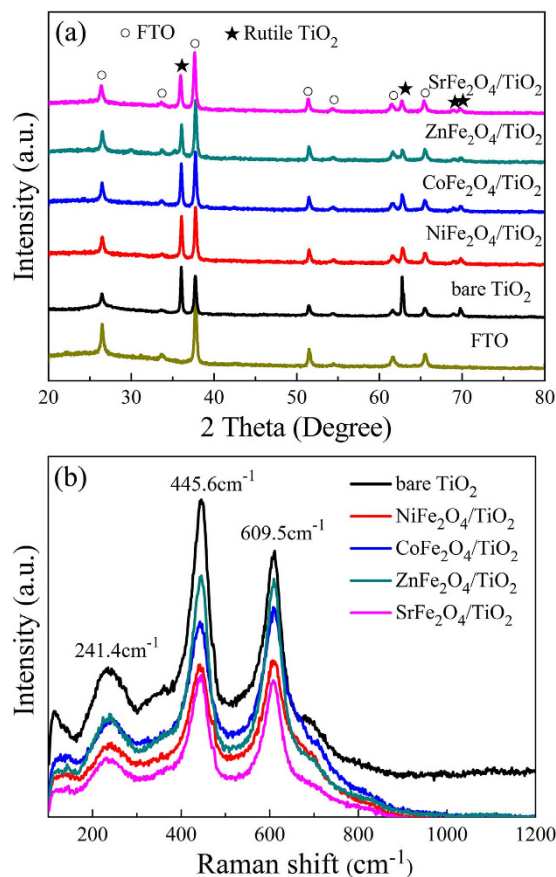
Figure 1. (**a**) XRD patterns and (**b**) Raman spectra for TiO_2 NRAs and MFe_2O_4/TiO_2 NRAs.

spectra indicate that Zn^{2+} exists in the $ZnFe_2O_4/TiO_2$ NRAs, which is also consistent with literature reports[34,35]. Furthermore, the manganese valences were determined by the position of the multiplet splitting of Sr 2p peaks, the positions of Sr 2p3/2 and Sr 2p1/2 were all assigned to Sr^{2+}. As for high-resolution XPS spectra of Fe 2p in Fig. 2(d), one can see that the peaks at *ca.* 711.6 eV and *ca.* 724.9 eV can be attributed to Fe 2p3/2 and Fe 2p1/2 for Fe^{3+}, respectively, which reveals the oxidation state of Fe^{3+} in the MFe_2O_4/TiO_2 heterostructure[33,36].

The high resolution XPS spectra of Ti 2p, O 1s, and C 1s are shown in Fig. 3. The Ti 2p spectra, as presented in Fig. 3(a), all show the main peak located at *ca.* 458.5 eV and *ca.* 464.2 eV, which can be attributed to Ti 2p3/2 and Ti 2p1/2 in TiO_2, respectively[37]. It is clear that the O 1s spectra of these MFe_2O_4/TiO_2 NRAs samples can be deconvoluted into two components centered at *ca.* 529.8 eV and *ca.* 531.4 eV using two Gaussian curve fittings {Fig. 3(b)}, The components at the lower and higher binding energy side can be assigned to the crystal lattice oxygen of TiO_2 and MFe_2O_4 and chemisorbed oxygen in a defective lattice site (i.e.–OH), respectively[32,38–41]. It is suggested that the hydroxyl group can capture the photogenerated holes and form highly reactive hydroxyl free radicals, which plays an important role in enhancing photocatalytic activity[18]. The high resolution XPS spectrum of C 1s is shown in Fig. 3(c). The primary peak located at *ca.* 284.6 eV is assigned to C–C/C–H bonds from adventitious carbon[42], while the peaks at *ca.* 286.2 eV and *ca.* 288.4 eV can be attributed to the formation of carbonate species, resulting mainly from CO_2 adsorption[38,43–45]. Especially, the peak at 288.4 eV can be ascribed to the Ti–O–C structure in carbon doped TiO_2 by substituting some of the lattice titanium atoms[46–48]. Interestingly, carbon doping is beneficial to light absorption capability as well as absorption of organic molecules to some extent[24,25].

The SEM images of the bare TiO_2 NRAs and MFe_2O_4/TiO_2 NRAs are shown in Fig. 4. It is noteworthy that, after MFe_2O_4 modification as shown in Fig. 4(c–f) from the top view images, the samples have no obvious changes in morphology compared with the bare TiO_2 NRAs in Fig. 4(a), which indicates that the deposited MFe_2O_4 nanoparticles are of extremely fine size. The vertically or slantingly aligned TiO_2 nanorods arrays, with diameter of 60~120 nm and length of 2.2 μm, are grown homogeneously on FTO substrate with rectangular cross section. In order to measure the content of MFe_2O_4 in MFe_2O_4/TiO_2 NRAs heterjunction, energy dispersive x-ray spectrum (EDS) analysis was carried out. The results, shown in Fig. 4(g~j), are obtained from collecting the EDS data in red square region of the MFe_2O_4/TiO_2 NRAs in Fig. 4(c–f), respectively. It is confirmed that Ni, Co, Zn and Sr are present in $NiFe_2O_4$, $CoFe_2O_4$, $ZnFe_2O_4$ and $SrFe_2O_4$ modified TiO_2 NRAs, respectively. Indeed, only a trace amount of Ni, Co, Zn and Sr can be observed in these samples.

Furthermore, structural characterizations of the MFe_2O_4 modified TiO_2 nanorods were investigated by TEM. Figure 5(a) shows the TEM image of the bare TiO_2 nanorod. Essentially, the diameter of the bare TiO_2 nanorod under TEM observation is consistent with the SEM result. It can be seen clearly that the bare TiO_2 nanorod is very
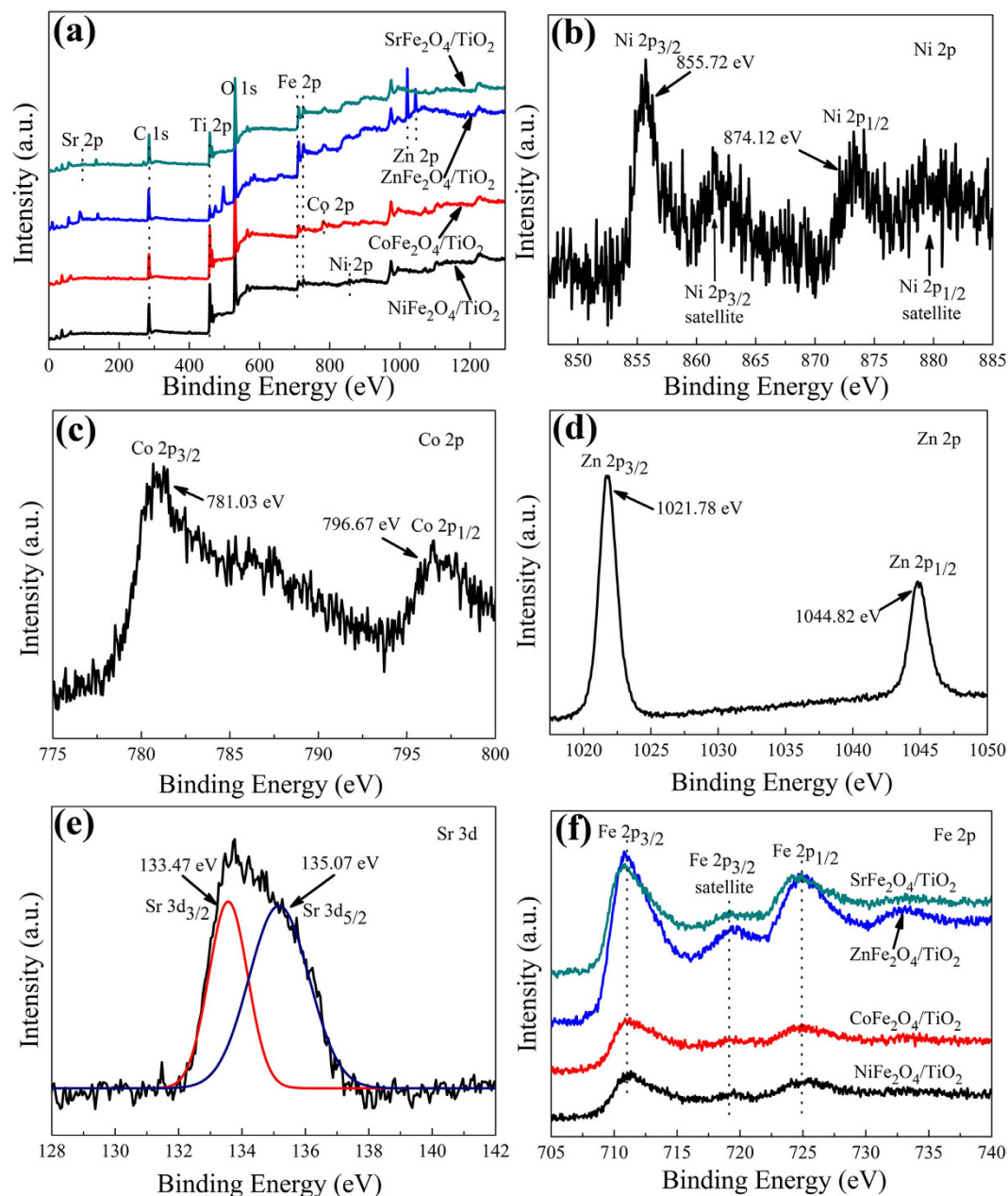
Figure 2. (**a**) XPS survey spectra of MFe_2O_4/TiO_2 NRAs and high-resolution XPS spectra of (**b**) Ni 2p, (**c**) Co 2p, (**d**) Zn 2p, (**e**) Sr 2p and (**f**) Fe 2p.

smooth. After MFe_2O_4 modification shown in Fig. 5(c), the nanorod surface becomes rough, and the ultrafine $NiFe_2O_4$ particles, with diameter of *ca*. 3~5 nm as shown in Fig. 5(d), are uniformly deposited on the nanorod. In addition, the high resolution HRTEM image gives lattice fringes of about 0.481 nm and 0.251 nm, corresponding to the d (111) and d (311) space of $NiFe_2O_4$, respectively. Analysis of TEM was also applied to $CoFe_2O_4$, $ZnFe_2O_4$ and $SrFe_2O_4$ modified TiO_2 NRAs (shown in Supplementary Fig. S1), and all show the same morphology. i.e., the smooth surface of TiO_2 nanorod become rough after MFe_2O_4 modification. The corresponding lattice fringes of $CoFe_2O_4$, $ZnFe_2O_4$ and $SrFe_2O_4$ are shown in Figure S1(b,d,f), respectively.

The optical absorption spectra of TiO_2 NRAs and MFe_2O_4/TiO_2 NRAs are shown in Fig. 6. All samples exhibit typical UV absorption ($\lambda < 380$ nm). It is noteworthy that, compared with bare TiO_2 NRAs, all MFe_2O_4/TiO_2 samples exhibit strong light absorption in a wide region from 380 nm to 900 nm, which can be attributed to the intrinsic band gap absorption of MFe_2O_4. However, unlike other pure TiO_2, tiny absorption of the as-prepared TiO_2 sample in the visible light range can be observed. There are two reasons accounting for this abnormal phenomenon, one is the scattering of light caused by the nanorod arrays, and the other is the impurity doping during the hydrothermal and sintering process[49–51]. The absorption capacity of $CoFe_2O_4/TiO_2$ NRAs is the biggest, followed by $ZnFe_2O_4$, $SrFe_2O_4$ and $NiFe_2O_4$ modified TiO_2 NRAs sequentially. The corresponding band gaps are calculated from the plots of $E_g = 1240/\lambda$ by extrapolating the linear portion of absorbance to the wavelength
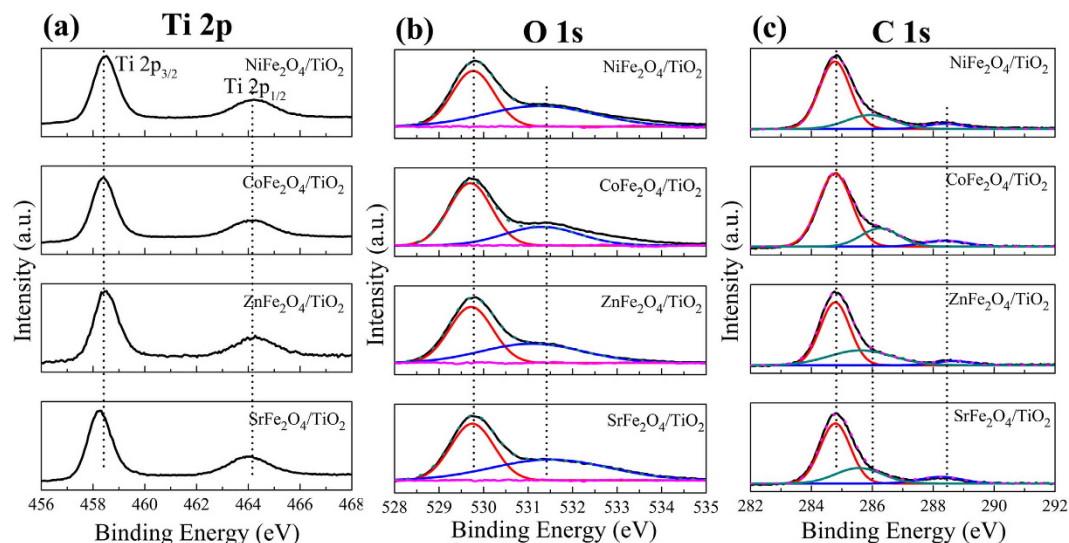
Figure 3. High-resolution XPS spectra of (**a**) Ti 2p, (**b**) O 1s and (**c**) C 1s.

axis where absorbance is zero[52]. As is shown in Fig. 6, the steep absorption edge of the bare TiO_2 NRAs locates at about 410 nm, corresponding to band gap (E_g) of about 3.02 eV. MFe_2O_4 modified TiO_2 NRAs samples all exhibit red-shift with smaller band gaps compared with bare TiO_2 NRAs, and the E_g is *ca.* 1.84 eV, 1.63 eV, 1.81 eV and 1.53 eV for $NiFe_2O_4/TiO_2$ NRAs, $ZnFe_2O_4/TiO_2$ NRAs, $SrFe_2O_4/TiO_2$ NRAs, and $CoFe_2O_4/TiO_2$ NRAs, respectively.

To evaluate the effect of MFe_2O_4 modification on the photoelectrochemical properties of TiO_2 NRAs, the photo-current intensity versus potential (*I–V*) and photocurrent density versus time (*I-T*) measurements of MFe_2O_4/TiO_2 NRAs were performed. The *I-V* characteristics of MFe_2O_4/TiO_2 NRAs are shown in Fig. 7(a). The photocur-rent density in dark can be neglected for all samples. Under visible light irradiation, the photocurrent density of bare TiO_2 NRAs varies little with increase in bias potential, while the photocurrent density of MFe_2O_4/TiO_2 NRAs increases significantly at more positive bias potentials, except for $CoFe_2O_4/TiO_2$ NRAs with only a slight increase. For example, at bias potential of 0.4 V vs. Ag/AgCl, the photocurrent density of $NiFe_2O_4$, $ZnFe_2O_4$ and $SrFe_2O_4$ modified TiO_2 NRAs is 6.13, 3.31 and 2.81 $\mu A/cm^2$, respectively, while the photocurrent density of $CoFe_2O_4/TiO_2$ NRAs is only 0.95 $\mu A/cm^2$, which is far lower than that of other MFe_2O_4 modified samples, and only a little higher than that of the bare TiO_2 NRAs (0.46 $\mu A/cm^2$ at 0.4 V vs. Ag/AgCl). It is reported that the more negative open circuit potential (Voc) means better charge carrier separation and electron accumulation in semiconductor-semiconductor heterojunctions[53–56]. After MFe_2O_4 modification, Voc for $NiFe_2O_4/TiO_2$ NRAs, $ZnFe_2O_4/TiO_2$ NRAs and $SrFe_2O_4/TiO_2$ NRAs is −0.323, −0.156 and −0.133 V, respectively, which becomes more negative than that of the bare TiO_2 NRAs (−0.121 V), except for $CoFe_2O_4$ modified one(−0.117 V). From the varying trend of Voc, one can see that MFe_2O_4/TiO_2 NRAs (M = Ni, Zn and Sr) heterjunction facilitates the separation and transfer of the charge carriers, while $CoFe_2O_4/TiO_2$ NRAs is not favourable for charge carriers separation. Figure 7(b) plots the *I-T* characteristics of the MFe_2O_4/TiO_2 NRAs. It is observed that all the samples exhibit a quick response to the on/off of the incident light, and the current density of MFe_2O_4 modified TiO_2 NRAs shows an enhancement compared with that of bare TiO_2 NRAs. $NiFe_2O_4/TiO_2$ NRAs displays the biggest photocurrent density of ca. 4.13 $\mu A/cm^2$, followed by $ZnFe_2O_4$, $SrFe_2O_4$ and $CoFe_2O_4$ modified ones, with 1.73, 1.68 and 1.01 $\mu A/cm^2$, respectively. The enhancement induced by $CoFe_2O_4$ modification is relatively low, only 0.4 $\mu A/cm^2$ higher than that of bare TiO_2 NRAs (0.61 $\mu A/cm^2$). The changing trend of *I-T* result is consistent with the *I-V* characteristics of the MFe_2O_4/TiO_2 NRAs.

Though all MFe_2O_4 modified TiO_2 NRAs samples exhibit a broader and stronger absorption than the bare TiO_2 NRAs (see Fig. 6), only $NiFe_2O_4/TiO_2$ NRAs possesses a significant enhancement in PEC performance. Very limited improvement for $CoFe_2O_4$ modification may result from the inefficient separation of photoexcited charge carriers. This phenomenon is due to the fact that the conduction band (CB) of $CoFe_2O_4$ is more positive than that of TiO_2, while the valence band (VB) of $CoFe_2O_4$ is more negative than that of TiO_2[41,57], which is not favour in carriers separating.

To investigate the photocatalytic capacity of the MFe_2O_4/TiO_2 NRAs, experiments were carried out for Cr(VI) photoreduction under visible light irradiation. The concentration changes are detected by the absorption peak (365 nm) of Cr(VI) in the UV-vis spectrum. The photodegradation results are shown in Fig. 7(c). After irradia-tion for 180 minutes, little Cr(VI) was reduced without catalyst (the reduction rate is only 3.8%). Under the same condition, only 45.1% of Cr(VI) was reduced when bare TiO_2 NRAs was used as a photocatalyst. However, the potoreduction capacity of $NiFe_2O_4$, $ZnFe_2O_4$ and $SrFe_2O_4$ modified TiO_2 NRAs are enhanced greatly (94.18%, 94.086% and 92.39%, respectively), reaching the same level. This may be attributed to the function of citric acid serving as a sacrificial electron donator to quickly consume the photogenerated holes[19], thus greatly promote charge separation and further improv photocatalytic reactions. Unfortunately, $CoFe_2O_4$ modification makes the photocatalytic degradation rate of Cr(VI) even lower. The following reason may account for this abnormal
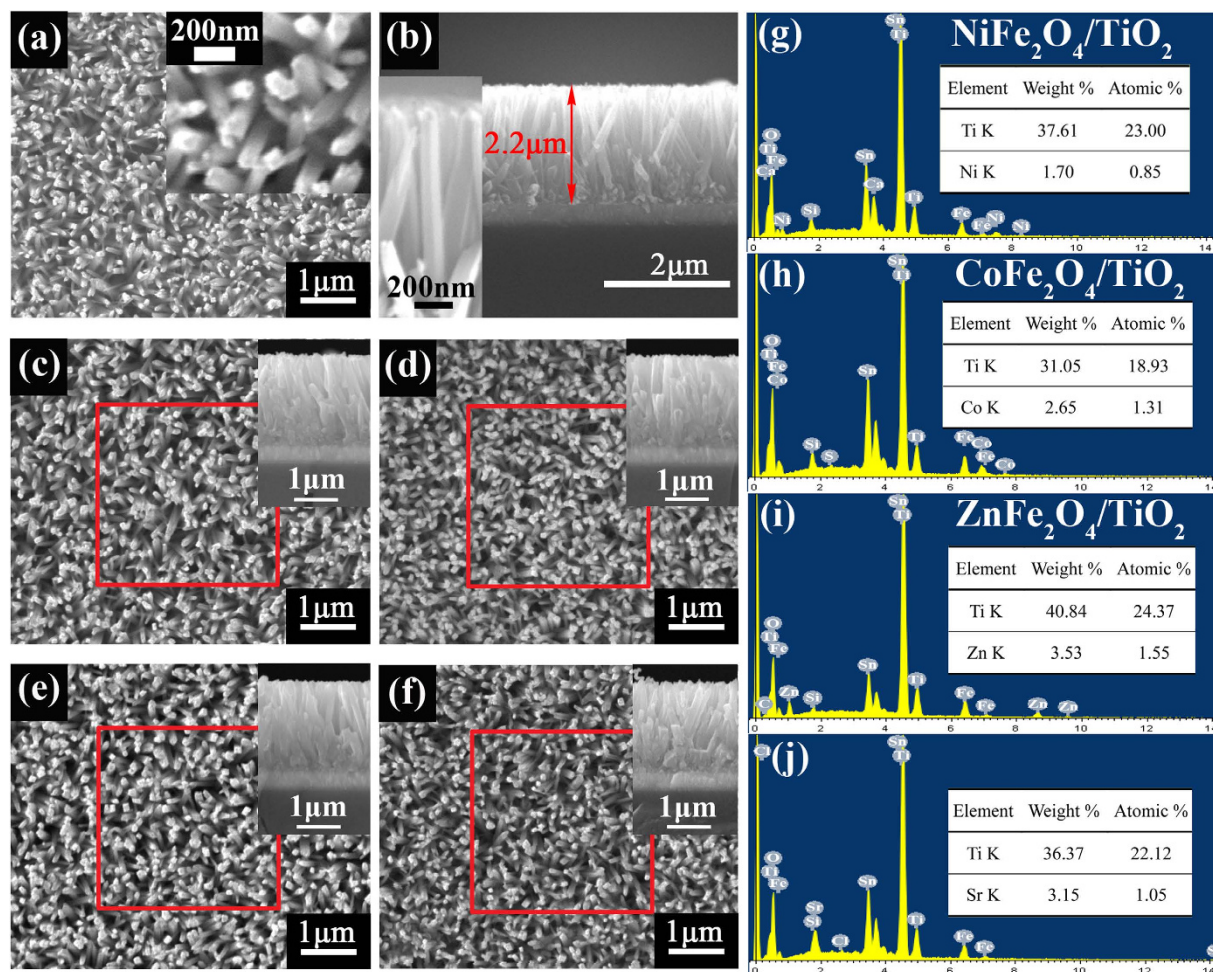
Figure 4. SEM images of (**a**) the bare TiO$_2$ NRAs, (**b**) the cross section image of the bare TiO$_2$ NRAs, (**c**) NiFe$_2$O$_4$/TiO$_2$ NRAs, (**d**) CoFe$_2$O$_4$/TiO$_2$ NRAs, (**e**) ZnFe$_2$O$_4$/TiO$_2$ NRAs and (**f**) SrFe$_2$O$_4$/TiO$_2$ NRAs. The insets of (**c–f**) are the corresponding cross section images. (**h,i,g,k**) are the EDS results of the red square region in (**c–f**), respectively.

phenomenon. Eventhough CoFe$_2$O$_4$ modified TiO$_2$ NRAs can be excited more easily under visible light irradiation, and then generates more charge carriers, the recombination rate of CoFe$_2$O$_4$/TiO$_2$ NRAs seems to be higher than that of the bare TiO$_2$ NRAs which can be deduced from the Voc changes, thus leading to the lower photocatalytic capacity of CoFe$_2$O$_4$/TiO$_2$ NRAs.

In order to clarify the enhancement in the photoelectochemical and photocatalytic capacity of TiO$_2$ NRAs after MFe$_2$O$_4$ modification, it is important to figure out the separating and transferring efficiency of the charge carriers, so electrochemical impedance spectroscopy (EIS) measurements were conducted. As shown in Fig. 7(d), except for CoFe$_2$O$_4$/TiO$_2$ NRAs, other MFe$_2$O$_4$ modified TiO$_2$ NRAs samples all have a smaller arc radius compared with that of the bare TiO$_2$ NRAs. It is generally assumed that the smaller arc radius on the EIS Nyquist plot suggests a more effective separation of the photogenerated electron-hole pairs and a faster interfacial charge transfer[38,58]. From the EIS spectra, it can be seen clearly that NiFe$_2$O$_4$, ZnFe$_2$O$_4$ and SrFe$_2$O$_4$ modified TiO$_2$ NRAs have a smaller arc radius than the bare TiO$_2$ NRAs. It means that the charge carriers separate and transfer more effectively in NiFe$_2$O$_4$/TiO$_2$ NRAs, ZnFe$_2$O$_4$/TiO$_2$ NRAs and SrFe$_2$O$_4$/TiO$_2$ NRAs, thus leading to the significant enhancement of the photoelectochemical and photocatalytic capacity of the modified TiO$_2$ NRAs. While the arc radius of CoFe$_2$O$_4$/TiO$_2$ NRAs is even bigger than that of the bare TiO$_2$ NRAs, suggesting lower separating rate of charge carriers in CoFe$_2$O$_4$/TiO$_2$ NRAs and thus resulting in the limited enhancement of the photoelectochemical capacity and even decrease in photocatalytic performance. This EIS result of CoFe$_2$O$_4$/TiO$_2$ NRAs is in accordance with the Voc value of CoFe$_2$O$_4$/TiO$_2$ NRAs in the *I-V* curves as well as the deduction from the band matching between CoFe$_2$O$_4$ and TiO$_2$ in previous literature, that is, the CoFe$_2$O$_4$/TiO$_2$ heterojunction is not conducive to effective separation of carriers.

Photocatalytic schematic of Cr(VI) by MFe$_2$O$_4$/TiO$_2$ NRAs is shown in Fig. 8. Under visible light illumination, MFe$_2$O$_4$ is effectively excited to generate electrons and holes. Because the conduction band of MFe$_2$O$_4$ is more positive than that of TiO$_2$, the excited electrons can quickly transfer from MFe$_2$O$_4$ to the conduction band of TiO$_2$, whereas the generated holes accumulate in the valence band of MFe$_2$O$_4$. Consequently, the excited electron/hole
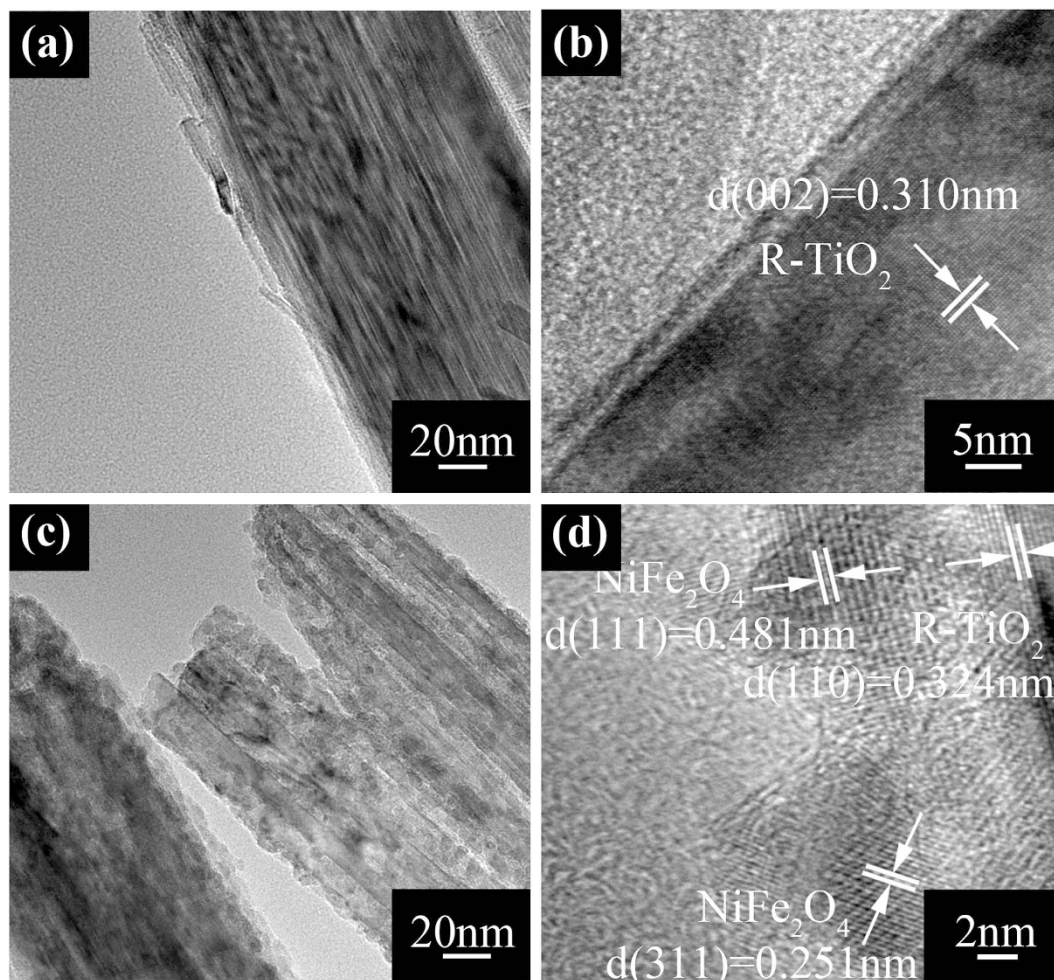
Figure 5. (**a,b**) TEM images of TiO$_2$ NRAs, (**c,d**) TEM images of NiFe$_2$O$_4$/TiO$_2$ NRAs.
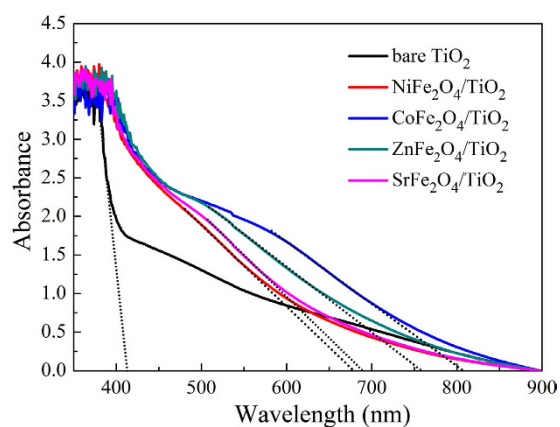
Figure 6. Absorption spectra of MFe$_2$O$_4$/TiO$_2$ NRAs. The dash lines are the extension of the linear portion of absorbance.

pairs could be separated effectively, which contributes to the improvement of photoelectrochemical properties of MFe$_2$O$_4$/TiO$_2$ NRAs, except for CoFe$_2$O$_4$/TiO$_2$ NRAs. Due to the efficient separation of the photogenerated electrons and holes by MFe$_2$O$_4$ modification, the lifetime of the charge carriers are prolonged, leading to an efficient oxidation-reduction reaction, so the photodegradation activity can be enhanced. When the photoreduction is carried out in the presence of citric acid, it can quickly consume the accumulated holes in the valence band, and thus the electrons in the conduction band have enough time to function with the Cr(VI) in the aqueous solution.
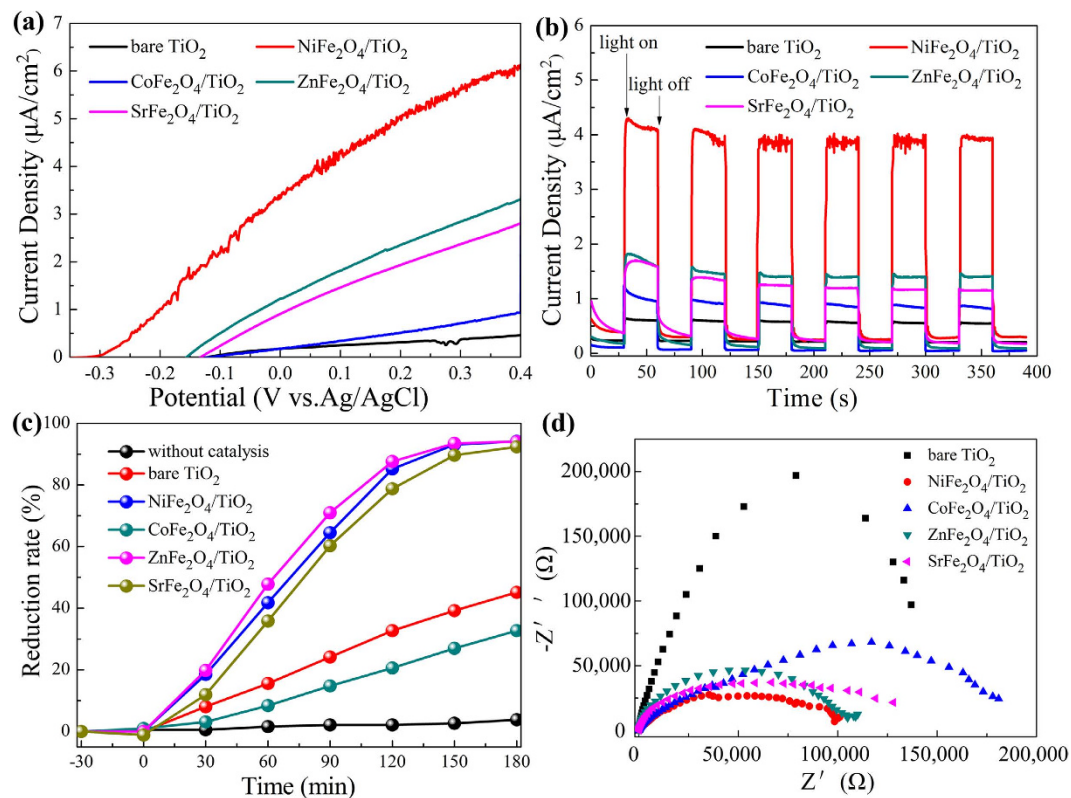
Figure 7. (**a**) Photocurrent density versus potential of the MFe$_2$O$_4$/TiO$_2$ NRAs, (**b**) Photocurrent density versus time measurements of MFe$_2$O$_4$/TiO$_2$ NRAs under 0 V versus Ag/AgCl bias, (**c**) Photocatalytic reduction of Cr(VI) by MFe$_2$O$_4$/TiO$_2$ NRAs under visible light, (**d**) Nyquist plots of the EIS spectra of MFe$_2$O$_4$/TiO$_2$ NRAs.
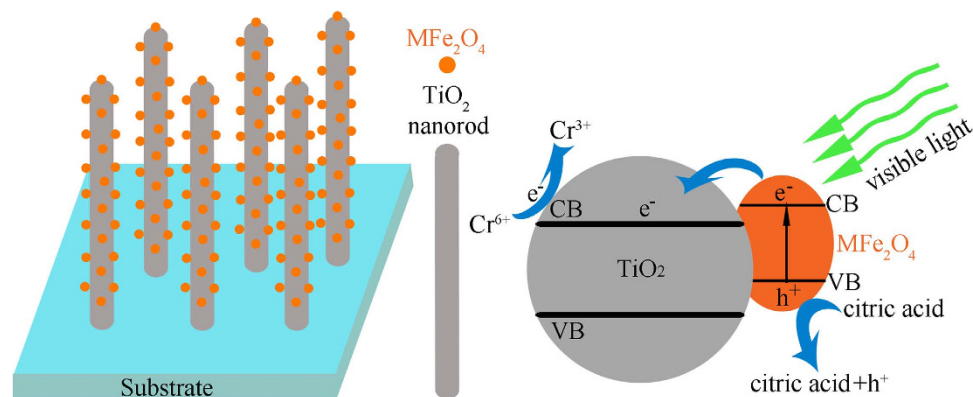
Figure 8. Photocatalytic schematic of Cr(VI) by MFe$_2$O$_4$/TiO$_2$ NRAs.

Conclusions

The effect of different ferrits (MFe$_2$O$_4$, M = Ni, Co, Zn and Sr) modification on improving the photoelectrochemical and photocatalytic properties of TiO$_2$ have been probed. By changing the incorporated cations in the MFe$_2$O$_4$, we have found that NiFe$_2$O$_4$ modification can greatly enhance the photoelectrochemical and photocatalytic performance of TiO$_2$ NRAs, while CoFe$_2$O$_4$ has relative limited effect. Compared with the bare TiO$_2$ NRAs, the photocurrent density of NiFe$_2$O$_4$/TiO$_2$ NRAs is twelve-fold higher in the I-V curve at 0.4 V vs. Ag/AgCl. Under visible light irradiation, the Cr(VI) photoreduction rate of NiFe$_2$O$_4$/TiO$_2$ NRAs achieves one-fold higher than that of the bare TiO$_2$ NRAs. The EIS measurement provides a clearer understanding of the role that MFe$_2$O$_4$ have in photogenerated charge carriers effectively separating and transferring. Except for CoFe$_2$O$_4$/TiO$_2$ NRAs, other MFe$_2$O$_4$ modified TiO$_2$ NRAs have more effective separation and transfer of the charge carriers, thus leading to the difference in the photoelectrochemical and photocatalytic performance of MFe$_2$O$_4$ modified TiO$_2$ NRAs. The obtained results point that the visible active MFe$_2$O$_4$ modification may be a promising way to improve TiO$_2$ for applications in photocatalytic activity as well as in photoelectrochemical conversion with solar light.

Methods

Materials synthesis.   All reagents used were analytical grade chemicals and used without further treatment.

Synthesis of MFe$_2$O$_4$ modified TiO$_2$ nanorod arrays.   Aligned TiO$_2$ NRAs were vertically grown on transparent fluorine-doped tin oxide (FTO) substrates by the hydrothermal method. Deionized water (DI, 10 mL) was mixed with hydrochloric acid (36.8 wt%, 10 mL) and stirred for 10 min before tetrabutyl titanate (98%, 0.4 mL) was added. When the solution was stirred until clear clarification, it was transferred to a Teflon-lined stainless steel autoclave. Clean FTO substrates were immersed with the conducting side face down. The autoclave was put in an oven at a temperature of 150 °C and was taken out from the oven after 5 h. After the autoclave was cooled to room temperature, the FTO substrate was rinsed with DI water and dried naturally at room temperature. The final area of the nanorod arrays was approximately 4.5 cm^2.

For the preparation of ZnFe$_2$O$_4$/TiO$_2$ NRAs, briefly, zinc nitrate and iron nitrate were dissolved in DI water at room temperature to form a mixture, the as-prepared TiO$_2$ NRAs were soaked in the Fe(NO$_3$)$_3$ and Zn(NO$_3$)$_2$ mixed solution (with concentrations of 0.25 M and 0.125 M, respectively) for 1 h, followed by dipping in DI water for 5 s. Afterwards the nanorod arrays were dried in air for 24 h and then annealed at 500 °C in air for 2 h with heating and cooling rates of 5 °C·min^{-1}. The MFe$_2$O$_4$/TiO$_2$ NRs (M = Ni, Co and Sr) were prepared using the same method by replacing the zinc nitrate with other nitrate.

Characterization.   The surface morphology was obtained with a scanning electron microscopy (SEM, VEDAIIXMUINCN) equipped with an energy dispersive X-ray spectroscopy (EDS) system. The film microstructure was further characterized by transmission electron microscopy (TEM). X-ray diffraction (XRD, PANalytical) with Cu-Ka (λ = 0.15401 nm) was operated at 40 kV and 40 mA in a 2θ range of 20–80° at a scanning speed of 5° min^{-1} to characterize the crystal structure. Raman spectra were recorded at room temperature using a inVia Reflex Raman spectrometer under Ar$^+$ (532 nm) laser excitation. The optical properties were probed by a UV–vis spectrophotometer (UV1800, Shimadzu) with a FTO substrate as a blank. X-ray photoelectron spectroscopy (XPS) was obtained using a ESCALAB 250Xi (The binding energy of the XPS spectra was calibrated with the reference to the C 1s peak at 284.8 eV.)

Photoelectrochemical and photocatalytic measurement.   photoelectrochemical measurements were performed in a 250 mL quartz cell using a three-electrode configuration, including the prepared samples as working electrode, a Pt foil as counter electrode, a saturated Ag/AgCl as reference electrode, and 0.5 M Na$_2$SO$_4$ aqueous solution as an electrolyte. The working electrode was illuminated within an area of about 1.5 cm^2 at zero bias voltage versus the Ag/AgCl electrode under solar-simulated (AM 1.5 G filtered, 100 mW·cm^{-2}, CEL-HXF300) light sources with a UV cutoff filter (providing visible light with $\lambda \geq$ 420 nm). The electrochemical impedance spectroscopy (EIS) measurements were recorded by employing an AC voltage of 5 mV amplitude with the initial potencial at 0.4 v (vs. Ag/AgCl) over the frequency range from 100 kHz to 100 mHz without light illumination.

The Cr(VI) photoreduction was performed in a quartz cell. In the photoreduction experiments, 15 mL of aqueous solution containing 20 mg·L^{-1} of K$_2$Cr$_2$O$_7$ and 85 mg·L^{-1} of citric acid was used. The citric acid served as a sacrificial electron donor. Prior to irradiation, the photocatalyst (area about 6 cm^2) was immersed into the Cr(VI) solution in the dark for 30 minutes to establish an adsorption/desorption equilibrium. The relative concentration of Cr(VI) in the solution was derived by comparing its UV–vis absorption intensity with that of the initial Cr(VI) solution at 365 nm. The light source was a 300 W xenon lamp with visible light illumination of 26.5 mW·cm^{-2}.

References

1. Yuan, R. *et al.* Surface Chlorination of TiO$_2$-Based Photocatalysts: A Way to Remarkably Improve Photocatalytic Activity in Both UV and Visible Region. *ACS Catalysis* **1,** 200–206 (2011).
2. Wang, H., You, T., Shi, W., Li, J. & Guo, L. Au/TiO$_2$/Au as a Plasmonic Coupling Photocatalyst. *Journal of Physical Chemistry C* **116,** 6490–6494 (2012).
3. Desario, P. A. *et al.* Plasmonic enhancement of visible-light water splitting with Au-TiO$_2$ composite aerogels. *Nanoscale* **5,** 8073–8083 (2013).
4. Chen, X. & Mao, S. S. Titanium Dioxide Nanomaterials: Synthesis, Properties, Modifications, and Applications. *Chemical Reviews* **38,** 2891–2959 (2007).
5. R., A., T., M., T., O., K., A. & Y., T. Visible-light photocatalysis in nitrogen-doped titanium oxides. *Science* **293,** 269–271 (2001).
6. Zheng, X. *et al.* Enhanced photoelectrochemical and photocatalytic performance of TiO$_2$ nanorod arrays/CdS quantum dots by coating TiO$_2$ through atomic layer deposition. *Nano Energy* **11,** 400–408 (2014).
7. N., H. K., Bhojya, N. H. S., Prashanth, K. P. N. & R., V. Optical and Photocatalytic Properties of Solar Light Active Nd-Substituted Ni Ferrite Catalysts: For Environmental Protection. *ACS Sustainable Chem Eng* **1,** 1143–1153 (2013).
8. H., Z., S., Z., X., H. Y., L., W. & S., S. Monodisperse M$_{(x)}$Fe$_{(3-x)}$O$_4$ (M = Fe, Cu, Co, Mn) nanoparticles and their electrocatalysis for oxygen reduction reaction. *Nano Letters* **13,** 2947–2951 (2013).
9. Neburchilov, V., Wang, H., Martin, J. J. & Wei, Q. A review on air cathodes for zinc–air fuel cells. *Journal of Power Sources* **195,** 1271–1291 (2010).
10. Bai, C. *et al.* Core– Ring Structured NiCo$_2$O$_4$ Nanoplatelets: Synthesis, Characterization, and Electrocatalytic Applications. *Advanced Functional Materials* **18,** 1440–1447 (2008).
11. Yanguang, L., Panitat, H. & Yiying, W. Ni$_{(x)}$Co$_{(3-x)}$O$_4$ nanowire arrays for electrocatalytic oxygen evolution. *Advanced Materials* **22,** 1926–1929 (2010).
12. Scaife, D. E. Oxide semiconductors in photoelectrochemical conversion of solar energy. *Solar Energy* **25,** 41–54 (1980).
13. Wuyou, F. *et al.* Anatase TiO$_2$ nanolayer coating on cobalt ferrite nanoparticles for magnetic photocatalyst. *Materials Letters* **59,** 3530–3534 (2005).
14. Li, C. J., Wang, J. N., Wang, B., Gong, J. R. & Lin, Z. Direct formation of reusable TiO$_2$/CoFe$_2$O$_4$ heterogeneous photocatalytic fibers via two-spinneret electrospinning. *Journal of Nanoscience & Nanotechnology* **12,** 2496–2502 (2012).
15. Kim, H. S. *et al.* Synthesis of magnetically separable core@shell structured NiFe$_2$O$_4$ @TiO$_2$ nanomaterial and its use for photocatalytic hydrogen production by methanol/water splitting. *Chemical Engineering Journal* **243,** 272–279 (2014).

16. Yuan, Z., You, W., Jia, J. & Zhang, L. Optical Absorption Red Shift of Capped ZnFe$_2$O$_4$ Nanoparticle. *Chinese Physics Letters* **15,** 535–536 (1998).
17. Yuan, Z. H. & Zhang, L. D. Synthesis, characterization and photocatalyticactivity of ZnFe$_2$O$_4$/TiO$_2$ nanocomposite. *Journal of Materials Chemistry* **11,** 1265–1268 (2001).
18. Hou, Y., Li, X., Zhao, Q., Quan, X. & Chen, G. Electrochemically assisted photocatalytic degradation of 4-chlorophenol by ZnFe$_2$O$_4$-modified TiO$_2$ nanotube array electrode under visible light irradiation. *Environmental Science & Technology* **44,** 5098–5103 (2010).
19. Chen, L. *et al.* Surface photovoltage phase spectra for analysing the photogenerated charge transfer and photocatalytic activity of ZnFe$_2$O$_4$-TiO$_2$ nanotube arrays. *Physical Chemistry Chemical Physics* **15,** 14262–14269, doi: 10.1039/c3cp51850g (2013).
20. Pan, J. *et al.* Construction of Mn$_{0.5}$Zn$_{0.5}$Fe$_2$O$_4$ modified TiO$_2$ nanotube array nanocomposite electrodes and their photoelectrocatalytic performance in the degradation of 2,4-DCP. *Journal of Materials Chemistry C* **3** (2015).
21. Kezzim, A., Nasrallah, N., Abdi, A. & Trari, M. Visible light induced hydrogen on the novel hetero-system CuFe$_2$O$_4$/TiO$_2$. *Energy Conversion & Management* **52,** 2800–2806 (2011).
22. Zhang, L., He, Y., Wu, Y. & Wu, T. Photocatalytic degradation of RhB over MgFe$_2$O$_4$/TiO$_2$ composite materials. *Materials Science & Engineering B* **176,** 1497–1504 (2011).
23. Šutka, A. *et al.* Photocatalytic activity of anatase–nickel ferrite heterostructures. *Physica Status Solidi Applications & Materials* **212,** 796–803 (2015).
24. Zhou, W. One-dimensional single-crystalline Ti–O based nanostructures: properties, synthesis, modifications and applications. *Journal of Materials Chemistry* **20,** 5993–6008 (2010).
25. Z., S., J. H., K., Y., Z., D., A. & S. X., D. Morphology-controllable 1D-3D nanostructured TiO$_2$ bilayer photoanodes for dye-sensitized solar cells. *Chemical Communications* **49,** 966–968 (2013).
26. Sun, Z. Continually adjustable oriented 1D TiO$_2$ nanostructure arrays with controlled growth of morphology and their application in dye-sensitized solar cells. *Crystengcomm* **14,** 5472–5478 (2012).
27. Zhou, H., Qu, Y., Zeid, T. & Duan, X. Towards highly efficient photocatalysts using semiconductor nanoarchitectures. *Energy & Environmental Science* **5,** 6732–6743 (2012).
28. Zhang, J., Xiao, F. X., Xiao, G. & Liu, B. Self-assembly of a Ag nanoparticle-modified and graphene-wrapped TiO$_2$ nanobelt ternary heterostructure: surface charge tuning toward efficient photocatalysis. *Nanoscale* **6,** 11293–11302 (2014).
29. Wang, L., Zhang, X., Ma, Y., Yang, M. & Qi, Y. Rapid microwave-assisted hydrothermal synthesis of one-dimensional MoO$_3$ nanobelts. *Materials Letters* **164,** 623–626 (2015).
30. Ma, H. L. *et al.* Raman study of phase transformation of TiO$_2$ rutile single crystal irradiated by infrared femtosecond laser. *Applied surface science* **253,** 7497–7500 (2007).
31. Robert, T. D., Laude, L. D., Geskin, V. M., Lazzaroni, R. & Gouttebaron, R. Micro-Raman spectroscopy study of surface transformations induced by excimer laser irradiation of TiO$_2$. *Thin Solid Films* **440,** 268–277 (2003).
32. Ji, H. *et al.* Correction: Magnetic g-C$_3$N$_4$/NiFe$_2$O$_4$ hybrids with enhanced photocatalytic activity. *RSC Adv.* **5,** 64299–64299 (2015).
33. Hao, J. *et al.* In situ controllable growth of CoFe$_2$O$_4$ ferrite nanocubes on graphene for colorimetric detection of hydrogen peroxide. *Journal of Materials Chemistry A* **1,** 4352–4357 (2013).
34. Wu, S. Reduced graphene oxide anchored magnetic ZnFe$_2$O$_4$ nanoparticles with enhanced visible-light photocatalytic activity. *RSC Advances* **5,** 9069–9074 (2015).
35. Song, H. Preparation of ZnFe$_2$O$_4$ nanostructures and highly efficient visible-light-driven hydrogen generation with the assistance of nanoheterostructures. *Journal of Materials Chemistry A* **3,** 8353–8360 (2015).
36. Fu, M., Jiao, Q. & Zhao, Y. Preparation of NiFe$_2$O$_4$ nanorod–graphene composites via an ionic liquid assisted one-step hydrothermal approach and their microwave absorbing properties. *Journal of Materials Chemistry A* **1,** 5577–5586 (2013).
37. Wang, S. *et al.* Facile synthesis of nitrogen self-doped rutile TiO$_2$ nanorods. *CrystEngComm* **14,** 7672–7679 (2012).
38. Fang-Xing, X. *et al.* Spatially branched hierarchical ZnO nanorod-TiO$_2$ nanotube array heterostructures for versatile photocatalytic and photoelectrocatalytic applications: towards intimate integration of 1D-1D hybrid nanostructures. *Nanoscale* **6,** 14950–14961 (2014).
39. Cheng, X., Yu, X. & Xing, Z. Characterization and mechanism analysis of N doped TiO$_2$ with visible light response and its enhanced visible activity. *Applied surface science* **258,** 3244–3248 (2012).
40. Yanli, C. *et al.* Enhanced photoelectric performance of PbS/CdS quantum dot co-sensitized solar cells via hydrogenated TiO$_2$ nanorod arrays. *Chemical Communications* **50,** 9509–9512 (2014).
41. Singh, S. Reduced Graphene Oxide Coupled CdS/CoFe$_2$O$_4$ Ternary Nanohybrid for Enhanced Photocatalytic Activity and Stability: A Potential Role of Reduced Graphene Oxide as a Visible Light Responsive Photosensitizer. *Journal of Virology* **77,** 4139–4148 (2015).
42. Hongwei, B., Zhaoyang, L. & Darren Delai, S. Hierarchical ZnO/Cu "corn-like" materials with high photodegradation and antibacterial capability under visible light. *Physical Chemistry Chemical Physics* **13,** 6205–6210 (2011).
43. Xiao, F. X. *et al.* Spatially branched hierarchical ZnO nanorod-TiO$_2$ nanotube array heterostructures for versatile photocatalytic and photoelectrocatalytic applications: towards intimate integration of 1D-1D hybrid nanostructures. *Nanoscale* **6,** 14950–14961 (2014).
44. Zeng, H. C., Xie, F., Wong, K. C. & Mitchell, K. A. R. Insertion and Removal of Protons in Single-Crystal Orthorhombic Molybdenum Trioxide under H$_2$S/H$_2$ and O$_2$/N$_2$. *Chemistry of Materials* **14,** 1788–1796 (2002).
45. Xu, M. W. & Hua, C. Z. Sulfidation of Single Molecular Sheets of MoO$_3$ Pillared by Bipyridine in Nanohybrid MoO$_3$ (4,4′-bipyridyl)$_{0.5}$. *Chemistry of Materials* **15,** 433–442 (2003).
46. Qi, X. & Ouyang, L. Photocatalytic activity and hydroxyl radical formation of carbon-doped TiO$_2$ nanocrystalline: Effect of calcination temperature. *Chemical Engineering Journal* **148,** 248–253 (2009).
47. Li, Y., Hwang, D. S., Lee, N. H. & Kim, S. J. Synthesis and characterization of carbon-doped titania as an artificial solar light sensitive photocatalyst. *Chemical Physics Letters* **404,** 25–29 (2005).
48. Ren, W. *et al.* Low temperature preparation and visible light photocatalytic activity of mesoporous carbon-doped crystalline TiO$_2$. *Applied Catalysis B Environmental* **69,** 138–144 (2007).
49. Wei, G., Shen, Y., Boschloo, G., Hagfeldt, A. & Ma, T. Influence of nitrogen dopants on N-doped TiO$_2$ electrodes and their applications in dye-sensitized solar cells. *Electrochimica Acta* **56,** 4611–4617 (2011).
50. Dai, G., Yu, J. & Liu, G. Synthesis and Enhanced Visible-Light Photoelectrocatalytic Activity of p–n Junction BiOI/TiO$_2$ Nanotube Arrays. *Journal of Physical Chemistry C* **115,** 7339–7346 (2011).
51. Xu, P. *et al.* Visible-light-driven photocatalytic S- and C- codoped meso/nanoporous TiO$_2$. *Energy Environ Sci* **3,** 1128–1134 (2010).
52. Yang, Y. C. *et al.* Electrospun nanofibers of p-type BiFeO$_3$/n-type TiO$_2$ hetero-junctions with enhanced visible-light photocatalytic activity. *RSC Advances* **4,** 31941–31947 (2014).
53. Baker, D. R. & Kamat, P. V. Photosensitization of TiO$_2$ Nanostructures with CdS Quantum Dots: Particulate versus Tubular Support Architectures. *Advanced Functional Materials* **19,** 805–811 (2009).
54. Subramanian, V., Wolf, E. E. & Kamat, P. V. Green emission to probe photoinduced charging events in ZnO-Au nanoparticles. Charge distribution and Fermi-level equilibration. *Journal of Materials Chemistry B* **107,** 7479–7485 (2003).
55. And, M. J., Levanon, H. & Kamat, P. V. Charge Distribution between UV-Irradiated TiO$_2$ and Gold Nanoparticles: Determination of Shift in the Fermi Level. *Nano Letters* **3,** 353–358 (2003).
56. Wood, A., Giersig, M. & Mulvaney, P. Fermi Level Equilibration in Quantum Dot–Metal Nanojunctions†. *Journal of Physical Chemistry B* **105,** 8810–8815 (2001).

57. Kudo, A. & Miseki, Y. Heterogeneous photocatalyst materials for water splitting. *Chemical Society Reviews* **38,** 253–278 (2009).
58. Xuan, P. *et al.* Comparing Graphene-TiO$_2$ Nanowire and Graphene-TiO$_2$ Nanoparticle Composite Photocatalysts. *ACS Applied Materials & Interfaces* **4,** 3944–3950 (2012).

Acknowledgements

Author Contributions

X.G. and Z.X. designed the study, proposed the mechanism, and wrote the manuscript. X.G., Z.X. and Z.Z. performed the experiments, analyzed the data, and prepared figures. X.L. and X.W. gave many suggestions during this work process. All authors reviewed the manuscript.

Additional Information

Supplementary information accompanies this paper at http://www.nature.com/srep

Competing financial interests: The authors declare no competing financial interests.

How to cite this article: Gao, X. *et al.* Enhanced photoelectrochemical and photocatalytic behaviors of MFe$_2$O$_4$ (M = Ni, Co, Zn and Sr) modified TiO$_2$ nanorod arrays. *Sci. Rep.* **6**, 30543; doi: 10.1038/srep30543 (2016).